



# Role of intramolecular hydrogen bonds in promoting electron flow through amino acid and oligopeptide conjugates

Rafał Orłowski<sup>a,1</sup>, John A. Clark<sup>b,1</sup>, James B. Derr<sup>c</sup>, Eli M. Espinoza<sup>d,2</sup>, Maximilian F. Mayther<sup>d</sup>, Olga Staszewska-Krajewska<sup>a</sup>, Jay R. Winkler<sup>e</sup>, Hanna Jędrzejewska<sup>a</sup>, Agnieszka Szumna<sup>a</sup>, Harry B. Gray<sup>e,3</sup>, Valentine I. Vullev<sup>b,c,d,3</sup>, and Daniel T. Gryko<sup>a,3</sup>

<sup>a</sup>Institute of Organic Chemistry, Polish Academy of Sciences, 01-224 Warsaw, Poland; <sup>b</sup>Department of Bioengineering, University of California, Riverside, CA 92521; <sup>c</sup>Department of Biochemistry, University of California, Riverside, CA 92521; <sup>d</sup>Department of Chemistry, University of California, Riverside, CA 92521; and <sup>e</sup>Division of Chemistry and Chemical Engineering, California Institute of Technology, Pasadena, CA 91125

Contributed by Harry B. Gray, January 17, 2021 (sent for review December 28, 2020; reviewed by David N. Beratan and David I. Schuster)

Elucidating the factors that control charge transfer rates in relatively flexible conjugates is of importance for understanding energy flows in biology as well as assisting the design and construction of electronic devices. Here, we report ultrafast electron transfer (ET) and hole transfer (HT) between a corrole (Cor) donor linked to a perylene-diimide (PDI) acceptor by a tetrameric alanine (Ala)<sub>4</sub>. Selective photoexcitation of the donor and acceptor triggers subpicosecond and picosecond ET and HT. Replacement of the (Ala)<sub>4</sub> linker with either a single alanine or phenylalanine does not substantially affect the ET and HT kinetics. We infer that electronic coupling in these reactions is not mediated by tetrapeptide backbone nor by direct donor–acceptor interactions. Employing a combination of NMR, circular dichroism, and computational studies, we show that intramolecular hydrogen bonding brings the donor and the acceptor into proximity in a “scorpion-shaped” molecular architecture, thereby accounting for the unusually high ET and HT rates. Photoinduced charge transfer relies on a (Cor)NH<sup>+</sup>···O=C–NH<sup>+</sup>···O=C(PDI) electronic-coupling pathway involving two pivotal hydrogen bonds and a central amide group as a mediator. Our work provides guidelines for construction of effective donor–acceptor assemblies linked by long flexible bridges as well as insights into structural motifs for mediating ET and HT in proteins.

charge transfer | hydrogen bonding | corrole | folding | perylene diimide

Many vital biological processes, including photosynthesis (1, 2), enzyme catalysis (3–5), and DNA repair (6–9), rely on electron transfer (ET) through proteins and nucleic acids (10–12). As the redox centers and chromophores mediating charge transfer (CT) are normally separated by relatively long molecular distances (>1 nm), the rates of ET and hole transfer (HT) depend critically on the media between donors and acceptors. It follows that the folding of biopolymer backbones plays a key role in governing CT properties.

Owing to the complexities of studying ET processes in biomacromolecules, model systems composed of donor and acceptor units located at the termini of oligomeric bridges have been employed to gain insight into the factors that control the redox behavior of biological systems. The evolution of biomimetic and bioinspired molecular devices also has become a major driving force for such studies (13). Despite the inherent flexibility of natural biomolecular oligomers, rigid bridges are common for the myriad of synthetic CT systems (10, 14–19). The difficulty in accounting for conformational dynamics has plagued interpretations of CT through peptides (20–22) and foldamers (23–25).

Long-range ET through covalent bonds in donor–bridge–acceptor (DBA) complexes has been the subject of numerous investigations over the last 40 years (10–12, 26). Of particular interest has been work on rigidly linked donor–acceptor units in Ru-modified proteins that has provided experimentally validated

tunneling timetables for interpretation and prediction of ET rates in structurally characterized DBA systems (10). Theoretical work by Beratan and others (27) has shed light on the factors that control these couplings both in small molecular DBA complexes and Ru-proteins.

Less well understood are couplings through solvents and other noncovalent molecular assemblies, most especially those in DBA complexes that feature B-group hydrogen-bond interactions (28, 29). In work reported here, we employ amino acids and an oligopeptide as bridges in corrole (Cor)–peptide–perylene-diimide (PDI) DBA conjugates in order to elucidate the role of hydrogen bonds in mediating biomimetic ET reactions. Specifically, we focus attention on a tetrapeptide bridging group, (Ala)<sub>4</sub>, which if extended would separate D and A and greatly diminish through-bond coupling. For comparison purposes, we also have investigated related DBA systems, one with a single alanine (Ala), another with phenylalanine (Phe) (Fig. 1). Varying the number of bridging residues between one and four does not drastically alter the excited-state dynamics of the DBA conjugates. Here, we show that intramolecular hydrogen bonding opens efficient DBA electronic coupling pathways for these CT reactions.

## Significance

Long-range electron transfer pervades biology, chemistry, and engineering, as it is critical for life-sustaining processes, chemical transformations, energy conversion, as well as electronic and photonic technologies. Elucidating the factors that control the rates of long-range electron transfer remains an outstanding challenge, owing in part to the complexity of proteins and other macromolecular structures that mediate such processes. We have found that short peptides linking electron donors and acceptors can assume folds with intramolecular hydrogen bond interactions that provide electronic-coupling pathways for ultrafast charge transfer. Our work will assist designs of donor–acceptor systems for efficient energy conversion and storage.

Author contributions: R.O., V.I.V., and D.T.G. designed research; R.O., J.A.C., J.B.D., E.M.E., M.F.M., O.S.-K., and H.J. performed research; J.R.W., A.S., H.B.G., V.I.V., and D.T.G. analyzed data; and R.O., J.A.C., J.R.W., H.B.G., V.I.V., and D.T.G. wrote the paper.

Reviewers: D.N.B., Duke University; and D.I.S., New York University.

The authors declare no competing interest.

Published under the PNAS license.

<sup>1</sup>R.O. and J.A.C. contributed equally to this work.

<sup>2</sup>Present address: College of Bioengineering, University of California, Berkeley, CA 94720.

<sup>3</sup>To whom correspondence may be addressed. Email: hbgray@caltech.edu, vullev@ucr.edu, or dtgryko@icho.edu.pl.

This article contains supporting information online at <https://www.pnas.org/lookup/suppl/doi:10.1073/pnas.2026462118/-DCSupplemental>.

Published March 12, 2021.

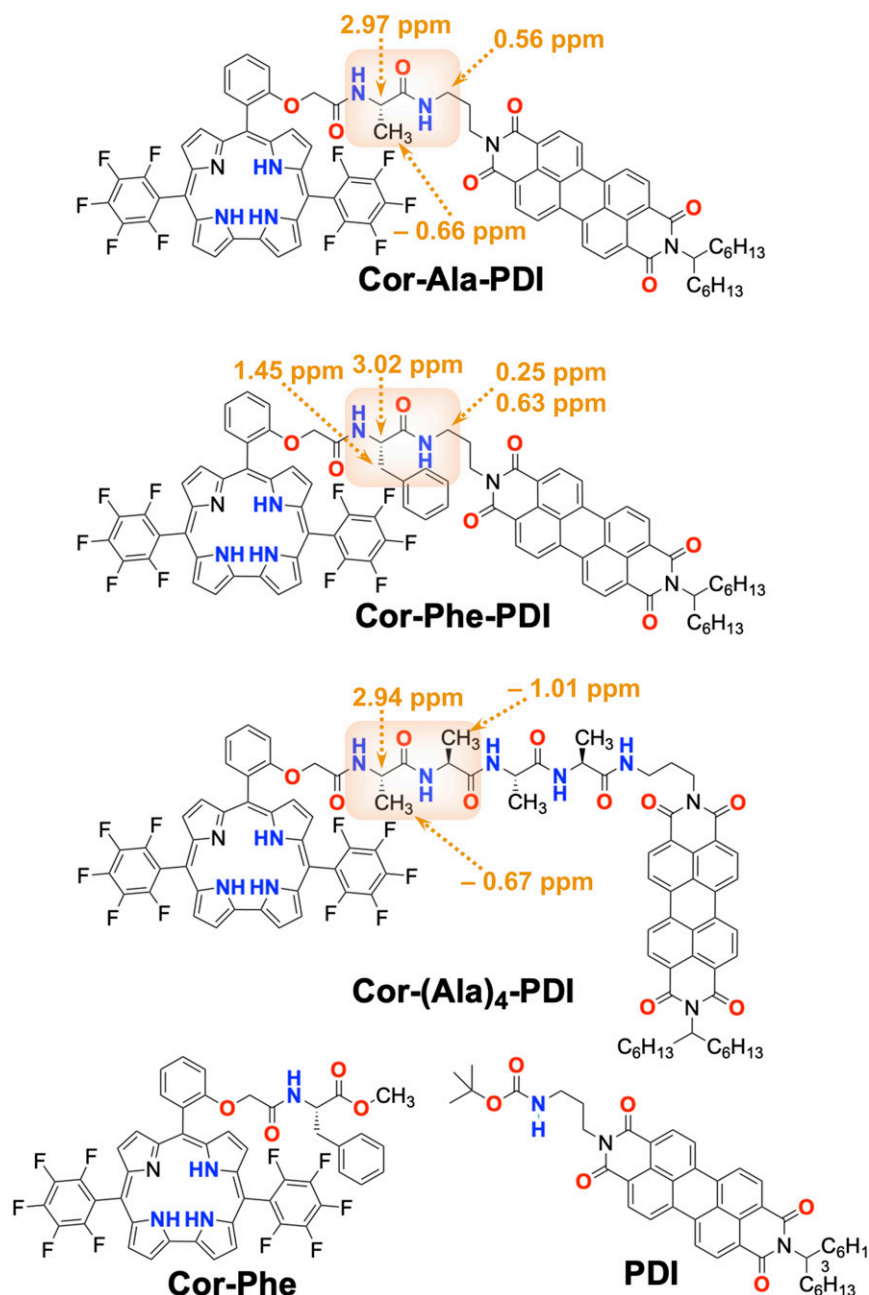


**Fig. 1.** Structures of DBA conjugates comprising a corrole derivative (Cor) as electron donor, a perylene-3,4,9,10-tetracarboxylic diimide (PDI) as electron acceptor, along with the Cor-Phe and PDI used for controls. The hydrogen-bond donors are highlighted in blue, and the hydrogen-bond acceptors are in red. The upfield-shifted chemical shifts, obtained from  $^1\text{H}$  NMR spectra, indicate sections of the bridge (highlighted) that are above the Cor macrocycle plane.

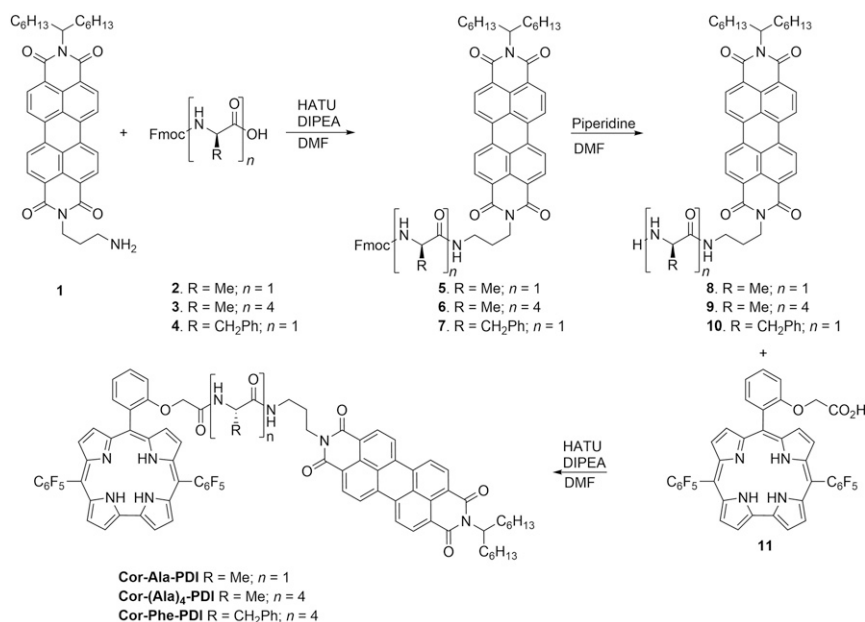
## Results

**Design and Synthesis.** The synthesis of the DBA complexes is outlined in Scheme 1. The design of these dyads is based on the following principles: 1) propensity of free-base corroles to form strong hydrogen bonds; 2) ability of short peptides to fold via intramolecular  $\text{C}=\text{O} \cdots \text{HN}$  hydrogen bonds; 3) the presence of  $\text{C}=\text{O}$  in PDI, which may contribute to the folding process via hydrogen bonds; 4) evidence from our earlier work that efficient ET occurs between corrole and PDI (30, 31).

The DBA complexes take advantage of a unique structural motif of amide-containing corroles that we recently discovered (32). Specifically, *trans*- $A_2B$ -corroles, bearing  $-\text{OCH}_2\text{CONHR}$  substituents at the *ortho* positions of the *meso*-phenyl group, exhibit a pronounced propensity for hydrogen bonding between

the amide carbonyl and corrole-NH (33). X-ray crystallography and NMR spectroscopy confirm this strong interaction between groups located at *meso*-10 position with the NH of the macrocyclic core in the solid state and in solution (32–34). This hydrogen bonding locks the amide group above the corrole cavity, resulting in pronounced upfield shifts of its proton NMR signals ( $\Delta\delta \sim -3$  ppm). Since this intramolecular hydrogen bonding perturbs the macrocycle structure, we use **Cor-Phe** as a model for the electron donor (Fig. 1). Critically important are the two electron-withdrawing  $\text{C}_6\text{F}_5$  groups at positions 5 and 15 that serve to stabilize the corrole core (35).

Our work on CT dyads of covalently linked Cor as an electron donor and PDI as an electron acceptor (30, 31) guided the choice for DBA scaffolds (Fig. 2). Selective excitation of Cor at



Scheme 1. Steps in the syntheses of Cor-Ala-PDI, Cor-(Ala)<sub>4</sub>-PDI, and Cor-Phe-PDI.

its Soret band between 390 and 440 nm or at wavelengths longer than 570 nm triggers ET to the acceptor; and excitation of PDI in the 460- to 530-nm region where Cor absorbs  $\leq 10\%$  of the light induces HT to the donor (Fig. 3). Moreover, the large overlap of PDI fluorescence and Cor absorption create the potential for Förster resonance energy transfer (EnT) from the excited PDI to Cor ( $R_0 = 46 \text{ \AA}$  assuming random orientation) (36).

The tetrapeptide bridge in the Cor-(Ala)<sub>4</sub>-PDI DBA conjugate provides two important features. 1) Adding 12 covalent bonds to an electronic-coupling pathway along the peptide backbone should decrease the CT rate constant ( $k_{CT}$ ) by more than five orders of magnitude (37), ensuring that any alternative short pathway, composed of hydrogen bonds or van der Waals contacts, would dominate the CT kinetics. 2) Alanine oligomers usually fold into helical loops that tend to have 3<sub>10</sub>-helix hydrogen-bonded configurations for short sequences (38–40). We would like to know whether intramolecular hydrogen bonding with the donor and the acceptor alters the propensity for formation of such 3<sub>10</sub>-helix patterns.

Shortening the (Ala)<sub>4</sub> bridge to a single residue (Ala, Phe) should increase the rates of through-bond CT. Therefore, the Cor-Ala-PDI conjugate (Fig. 1) serves as a control to test for contributions from through-bond coupling pathways to the CT kinetics. The side chains can play a role in protein CT by providing electronic-coupling pathways (41–43) and steric hindrance that preferentially tightens some of the conformational folds.

The phenyl group in the bridge of the Cor-Phe-PDI DBA conjugate provides a means to test for such effects.

**NMR Spectra.** Our recent studies of self-organization in *trans*-A<sub>2</sub>B-corroles bearing –OCH<sub>2</sub>CONHR groups at the *ortho* position of the *meso*-phenyl substituent revealed the propensity for intramolecular hydrogen bond formation between pyrrole NH groups and the oxygen of the amide carbonyl (26–28). Cor-Phe has 4 hydrogen-bond donors and 4 hydrogen-bond acceptors; Cor-Ala-PDI and Cor-Phe-PDI, 5 hydrogen-bond donors and 7 acceptors (2 of the 7 are on the distal end of PDI, however); and Cor-(Ala)<sub>4</sub>-PDI, 8 hydrogen-bond donors and 10 acceptors (Fig. 1). The high density of H-bonding groups, along with the flexibility of the bridges, make these conjugates highly prone to intramolecular hydrogen bonding, especially in nonpolar media. Amides possess large electric dipole moments (44) that can be stabilized by burial inside folded molecular structures in nonpolar media.

Analysis of <sup>1</sup>H NMR spectra, along with COSY, HSQC, and HMBC, revealed several key structural features. The <sup>1</sup>H and <sup>13</sup>C NMR spectra reveal that some linker resonances in Cor-Ala-PDI, Cor-Phe-PDI, and Cor-(Ala)<sub>4</sub>-PDI are shifted upfield by as much as –2.9 ppm from typical  $\delta$  values. Upfield shifts indicate protons in proximity of the magnetic dipole axis created by the corrole macrocyclic ring current induced by the external magnetic field. On the basis of the hydrogen-bonding propensity of the pyrroles

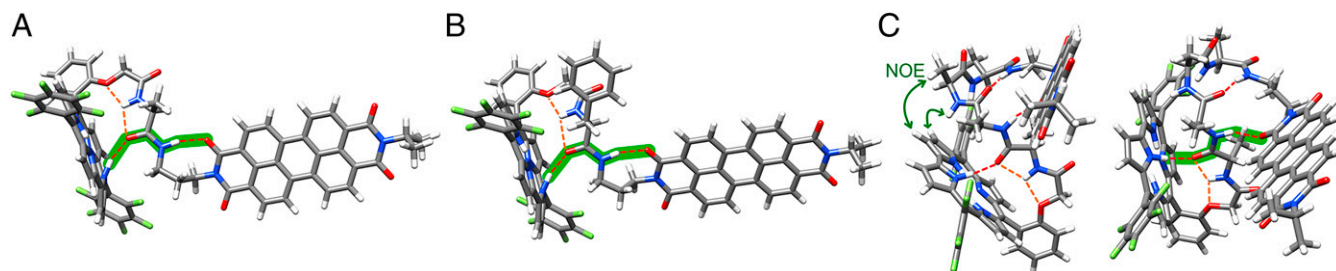
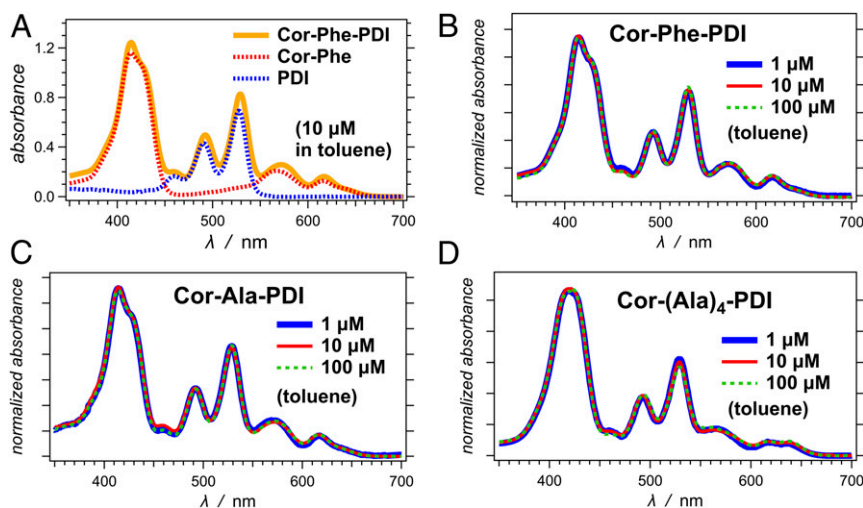


Fig. 2. Structures of (A) Cor-Ala-PDI, (B) Cor-Phe-PDI, and (C) Cor-(Ala)<sub>4</sub>-PDI (two views), with geometries optimized using DFT at the B3LYP/6-31G(d,p) level of theory for chloroform. Crucial stabilizing hydrogen-bonding interactions are marked with red dashed lines. The shortest through-bond donor-acceptor electronic coupling pathways, (Cor)NH...O=C-NH...O=C(PDI), are highlighted in green.



**Fig. 3.** Absorption spectra of the DBA conjugates. (A) Comparison of the spectra of **Cor-Phe-PDI** and its components, **Cor-Phe** and **PDI**. (B–D) Overlaid normalized absorption spectra of 1, 10, and 100  $\mu\text{M}$  of DBA conjugates in toluene. For measurements of 100  $\mu\text{M}$  samples, 0.1-mm cuvettes were used.

with linker carbonyls, we attribute the upfield-shifted resonances to protons located at similar distances from the corrole ring in the three DBA complexes (Figs. 1 and 2). Furthermore, ROESY spectra of **Cor-(Ala)<sub>4</sub>-PDI** exhibit through-space NOE correlations that indicate conformers in which some corrole-ring  $\beta$ -protons are in proximity to the methyl and the N-terminal amide of the third alanine (Fig. 2C).

**Optical Spectra.** The tendency of corroles to deprotonate in weakly basic polar media [e.g., nitriles, DMF (45)] dictated the choice of toluene as the solvent for ET investigations. The absorption spectra of the DBA conjugates in toluene are unchanged over a 1 to 100  $\mu\text{M}$  concentration range (Fig. 3), indicating that the Cor and PDI derivatives do not aggregate in toluene at micromolar concentrations. Incorporation of Cor and PDI into the DBA conjugates causes minor perturbations in their absorption spectra, predominantly in the bands of the Cor moiety (Fig. 3A). These small differences between the absorption spectra of Cor and the DBA conjugates are most pronounced for **Cor-(Ala)<sub>4</sub>-PDI** (Fig. 3). We ascribe these subtle variations in the spectra to intramolecular interactions, such as hydrogen bonding, because of the lack of concentration dependence of the optical spectra (Fig. 3 B–D). The absence of significant broadening and CT absorption precludes  $\pi$ -stacking between the donor and the acceptor. Furthermore, the lack of apparent CT absorption bands in the DBA spectra indicates weak donor–acceptor electronic coupling.

Attaching even a single amino acid residue with a stereogenic carbon center to the corrole moiety (e.g., **Cor-Phe**) introduces pronounced optical activity in the Soret region of the spectrum (Fig. 4). Adding PDI to the structures amplifies circular dichroism (CD) signals; and changing the Ala bridge to Phe further enhances the optical activity of the DBA conjugates (Fig. 4A and B). These findings suggest that the additional aromatic and PDI moieties tighten structures in conformers with preferred chirality.

The Soret CD spectra of **Cor-Phe**, **Cor-Ala-PDI**, and **Cor-Phe-PDI** exhibit negative Cotton effects originating from splitting of the Soret band: 1) at about 426 nm, dominating the CD signal; and 2) at the absorption maximum at about 413 nm, responsible for the hypsochromic CD shoulder (Fig. 4A and B). The sharp features in the **Cor-(Ala)<sub>4</sub>-PDI** Soret CD spectrum indicate a tighter structure with the tetrapeptide bridge.

**Computational Studies.** The NMR findings, and prior X-ray diffraction data (32–34), guide construction of computational models

of the DBA conjugates. Geometry optimization at the DFT/B3LYP/6-31G(d,p) level of theory with implementation of a PCM solvent model (46) yields structures that are consistent with the experimental findings (Figs. 1 and 2). For the structures containing single-residue linkers (**Cor-Ala-PDI**, **Cor-Phe-PDI**), the amino acid and first methylene group from the aliphatic linker lie above the corrole ring (Fig. 2A and B), consistent with upfield shifts of  $^1\text{H}$  NMR resonances for these groups (Fig. 1). Intramolecular hydrogen bonding between a pyrrole nitrogen proton and the C-terminal carbonyl of the amino acid, along with favorable interactions of the amide NH (from N terminus) with two oxygen atoms (one ethereal and the other carbonyl from the C terminus), stabilize a folded motif, leaving one carbonyl oxygen (an H-bond acceptor) and one amide hydrogen (an H-bond donor) available for further interactions. The calculations show that an additional engagement between the NH of the C-terminal amide of the amino acid and one of the PDI carbonyl oxygen atoms produces a conformer with an eight-bond ring that is energetically favorable in low-polarity media. In toluene, for example, hydrogen bonding and folding stabilize the DBA conjugate by 164 meV ( $6.5k_{\text{B}}T$  at  $T = 20^\circ\text{C}$ ). The folded structure brings the corrole and PDI to a center-to-center separation of 13.3 Å and creates an electronic-coupling pathway comprising two covalent and two hydrogen bonds [(Cor)NH $\cdots$ O=C–NH $\cdots$ O=C(PDI)] (Fig. 2A and B).

The **Cor-(Ala)<sub>4</sub>-PDI** DBA complex has considerably more conformational freedom. Owing to the upfield shifted resonances in the NMR spectrum, we constrained structural models for **Cor-(Ala)<sub>4</sub>-PDI** to have two alanine residues within the aromatic ring current of the corrole. The remaining two Ala residues admit a broad distribution of energetically accessible conformations. Our calculations suggest that in toluene two folded structures and one extended structure have energies within  $5k_{\text{B}}T$  of one another, spanning center-to-center distances of 12.7 to 19.8 Å (Fig. 2, also see *SI Appendix*). Among these structures, the shortest electronic coupling pathway has 2 covalent and 2 hydrogen bonds; the longest pathway is composed of 15 covalent bonds.

With the modeled structures in hand, we calculated CD spectra using time-dependent density-functional theory (TD-DFT). We initially treated the two chromophores separately with fragments of the amino acid bridge. Calculations for the PDI fragment indicate that hydrogen bonding with the amino acid induces CD with the same sign and shape as the band in the experimental spectrum (Fig. 4D). The calculations reproduce well the energies of the bands for the Cor fragment and demonstrate that the signs

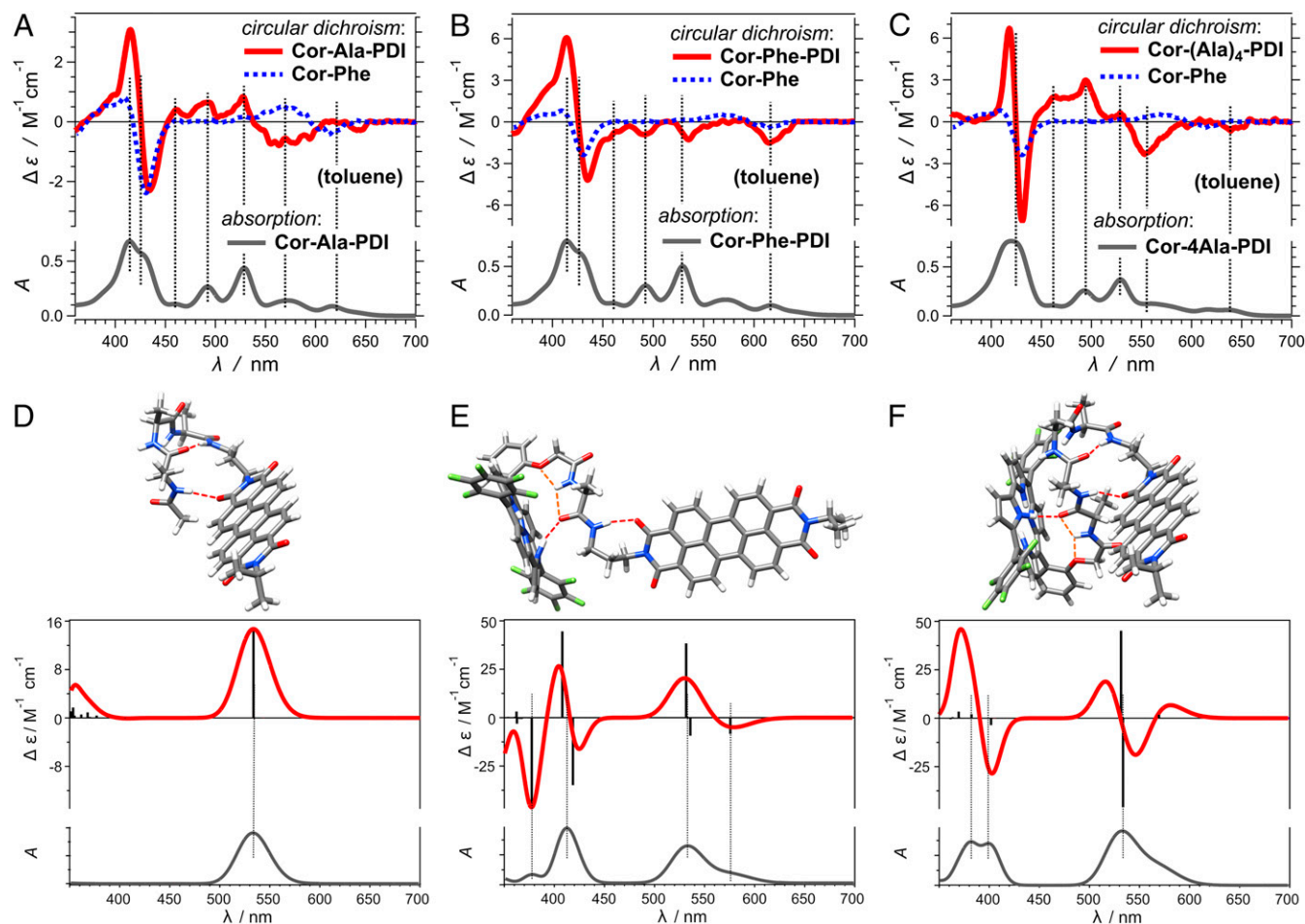


**Fig. 4.** (A–C) Experimental circular dichroism (CD) spectra of the three DBA conjugates in toluene, displayed with the CD spectrum of Cor-Phe. For comparison, ground-state absorption spectra of DBA compounds are displayed at the bottom of the panels. (D–F) Theoretically calculated CD and optical absorption spectra for (D) PDI linked with a “partial” bridge structure, i.e., **Ac-(Ala)<sub>3</sub>-PDI**; (E) **Cor-(Ala)-PDI**; and (F) **Cor-(Ala)<sub>4</sub>-PDI**. The structures, calculated using TD-DFT at the B3LYP/6-31G(d,p) level of theory for toluene, are shown above the corresponding panels with computed spectra.

of CD signals are sensitive to fine structural details. Armed with findings on the separate fragments, we proceeded to calculate CD spectra for the optimized geometries of **Cor-Ala-PDI** and **Cor-(Ala)<sub>4</sub>-PDI** (Fig. 4 E and F). The signs of the bands in the experimental and calculated spectra are in reasonable agreement, supporting the modeled folded structures containing the (Cor) NH<sup>+</sup>⋯O=C-NH<sup>+</sup>⋯O=C(PDI) motif in the three DBA conjugates.

**ET Thermodynamics.** The reduction potentials associated with Cor oxidation and PDI reduction [ $E_{\text{Cor}^{++}|\text{Cor}}^{(1/2)}$  and  $E_{\text{PDI}|\text{PDI}^{*-}}^{(1/2)}$ , respectively], along with their zero-to-zero excitation energies ( $\mathcal{E}_{00}$ ), allow estimation of the driving forces for photoinduced charge transfer (PCT) in media with different dielectric constants,  $\epsilon$  (47, 48):

$$\Delta G_{\text{PCT}}^{(0)}(\epsilon) = F \left( E_{\text{Cor}^{++}|\text{Cor}}^{(1/2)}(\epsilon_D) - E_{\text{PDI}|\text{PDI}^{*-}}^{(1/2)}(\epsilon_A) \right) - \mathcal{E}_{00} + \Delta G_S + W. \quad [1]$$

For  $\Delta G_{\text{ET}}^{(0)}$ ,  $\mathcal{E}_{00} = \mathcal{E}_{00}^{(\text{Cor})}$ ; and for  $\Delta G_{\text{HT}}^{(0)}$ ,  $\mathcal{E}_{00} = \mathcal{E}_{00}^{(\text{PDI})}$ . While toluene is the medium of choice for these photoinduced CT studies, relatively polar media, with dielectric constants  $\epsilon_D$  and  $\epsilon_A$ , are essential for electrochemical determination of  $E_{\text{Cor}^{++}|\text{Cor}}^{(1/2)}$  and  $E_{\text{PDI}|\text{PDI}^{*-}}^{(1/2)}$ , respectively. The Coulombic work term,  $W$ , accounts for the interaction between  $\text{Cor}^{++}$  and  $\text{PDI}^{*-}$ . For  $n$ -ET between a donor with an initial charge  $x$  and an acceptor with an initial charge  $y$ , the Born

solvation term,  $\Delta G_S$ , corrects for the differences between medium polarities for CT studies and electrochemical measurements (Eq. 2) (48, 49):

$$\Delta G_S = \frac{nq_e^2}{8\pi\epsilon_0} \left( \frac{2x+n}{r_D} \left( \frac{1}{\epsilon} - \frac{1}{\epsilon_D} \right) - \frac{2y-n}{r_A} \left( \frac{1}{\epsilon} - \frac{1}{\epsilon_A} \right) \right), \quad [2]$$

where  $q_e$  is the electron charge, and  $r_D$  and  $r_A$  are effective radii of the donor and acceptor, respectively.

Considering one-electron oxidation and reduction of noncharged donors and acceptors, i.e.,  $n = 1$  and  $x = y = 0$ , for identical electrochemical solvents, i.e.,  $\epsilon_D = \epsilon_A = \epsilon_E$ , simplifies the expression for the PCT driving force as well as the dependence of the potential differences,  $\Delta E_0^{(1/2)}(\epsilon) = E_{\text{Cor}^{++}|\text{Cor}}^{(1/2)}(\epsilon) - E_{\text{PDI}|\text{PDI}^{*-}}^{(1/2)}(\epsilon)$ , on the medium polarity as implemented by the Born solvation energy:

$$\Delta G_{\text{PCT}}^{(0)}(\epsilon) = F \Delta E_0^{(1/2)}(\epsilon) - \mathcal{E}_{00} + W, \quad [3a]$$

$$\Delta E_0^{(1/2)}(\epsilon) = \Delta E_0^{(1/2)}(\epsilon_E) + \frac{q_e^2}{8\pi\epsilon_0 F} S_{1/r} \left( \frac{1}{\epsilon} - \frac{1}{\epsilon_E} \right), \quad [3b]$$

where  $S_{1/r}$  is the sum of the inverse radii of the donor and acceptor:  $S_{1/r} = r_D^{-1} + r_A^{-1}$ .

The acidity of pyrrole protons in oxidized free-base corroles affects their electrochemical behavior (50, 51). The first one-electron

oxidation leads to triprotonated radical cations,  $\text{Cor}[\text{H}_3]^{3+}$ , that have increased acidity and readily protonate basic solvents, B, or other corroles within voltammetry timescales (milliseconds to seconds):  $\text{Cor}[\text{H}_3]^{3+} + \text{Cor}[\text{H}_3] \rightarrow \text{Cor}[\text{H}_2]^{2+} + \text{Cor}[\text{H}_4]^{4+}$ ;  $\text{Cor}[\text{H}_3]^{3+} + \text{B} \rightarrow \text{Cor}[\text{H}_2]^{2+} + \text{BH}^+$ . Positive-sweep cyclic voltammograms of free-base corroles, therefore, show anodic waves corresponding to the oxidations of  $\text{Cor}[\text{H}_4]^{4+}$  and  $\text{Cor}[\text{H}_2]^{2+}$  that closely follow the initial one-electron oxidation wave (51).

For a low-polarity solvent such as  $\text{CH}_2\text{Cl}_2$ , positive-sweep cyclic voltammograms of **Cor-Phe** show a well-defined anodic wave corresponding to the initial oxidation, with a peak potential at about 1 V vs. SCE (Fig. 5A). While occasionally a small cathodic peak around 0.85 V vs. SCE becomes detectable at low concentrations of supporting electrolyte,  $C_{el}$ , the oxidation of **Cor-Phe** tends to exhibit irreversibility at scan rates on the order of  $100 \text{ mV}\cdot\text{s}^{-1}$  (Fig. 5A). For irreversible oxidation, the inflection point of the first anodic wave provides an estimate for  $E_{\text{Cor}^{3+}|\text{Cor}}^{(1/2)}$  (52). Increasing solvent polarity not only causes negative shifts of the oxidation features in the voltammograms, but also broadens the first anodic wave and merges it with the waves that follow. An increase in electrolyte concentration also induces slight negative shifts in the reduction potentials of **Cor}^{3+}**-**Phe** (Fig. 5A). For each solvent, extrapolation to zero electrolyte concentration, i.e.,  $C_{el} = 0$ , allows estimation of the potentials for neat solvent,  $E_0^{(1/2)}$  (Fig. 5B) (53–55).

The cyclic voltammograms of **PDI** show two reversible reduction waves (Fig. 5A), consistent with previously reported electrochemical behavior for this chromophore (56). The mean of the first cathodic and anodic peak potentials provides estimates for  $E_{\text{PDI}|\text{PDI}^{•-}}^{(1/2)}$ . Combining the results for **PDI** and **Cor-Phe** for three different solvents allows an estimation of the potential difference

$\Delta E_0^{(1/2)}$  for toluene from the linear fit of  $\Delta E_0^{(1/2)}(\epsilon)$  vs.  $\epsilon^{-1}$ :  $S_{1/2} = 0.36 \pm 0.07 \text{ \AA}^{-1}$ , and  $\Delta E_0^{(1/2)}(\epsilon_{\text{toluene}}) = 2.3 \pm 0.1 \text{ eV}$  (Fig. 5C and Eq. 3b). The uncertainty indicated by the shading around the curves for  $\Delta G_{\text{CT}}^{(0)}$  (Fig. 5C) originates from the uncertainty in estimating  $\Delta E_0^{(1/2)}$  in toluene.

The estimated  $\Delta E_0^{(1/2)}$  in toluene simplifies the calculations of CT driving forces pertinent to this study (Eq. 3a). The dependence of the Coulombic term,  $W$  (Eqs. 1 and 3a), on the center-to-center donor–acceptor distance,  $R_{\text{DA}}$ , which is especially pronounced for nonpolar media (57), can induce variations in  $\Delta G_{\text{CT}}^{(0)}$  that amount to half an eV (Fig. 5D). An increase in  $R_{\text{DA}}$  causes negative shifts in  $\Delta G_{\text{ET}}^{(0)}$  and  $\Delta G_{\text{HT}}^{(0)}$ , and a positive shift in  $\Delta G_{\text{CR}}^{(0)}$  (Fig. 5D). For a center-to-center distance between **PDI** and **Cor** exceeding about  $20 \text{ \AA}$ ,  $\Delta G_{\text{ET}}^{(0)}$  assumes positive values such that ET is unfavorable. Conversely,  $\Delta G_{\text{HT}}^{(0)}$  and  $\Delta G_{\text{CR}}^{(0)}$  are negative over the entire  $R_{\text{DA}}$  range (Fig. 5D).

**Excited-State Dynamics.** Electrochemical and photophysical analyses of **Cor-Phe** and **PDI** reveal favorable thermodynamics for the formation of a CT state,  $\text{Cor}^{2+}\text{-PDI}^{\bullet-}$ , via multiple pathways (Scheme 2). Whether CT reactions can compete with deactivation of locally excited (LE) states ( $^1\text{Cor}^*$ ,  $^1\text{PDI}^*$ ), however, depends on the strengths of electronic couplings within the amino acid linkers.

**Cor** and **PDI** fluorescence quantum yields ( $\phi_f$ ) indicate accelerated excited-state decay when incorporated in DBA conjugates. Selective **Cor** ( $\lambda_{\text{ex}} = 620 \text{ nm}$ ) or **PDI** excitation ( $\lambda_{\text{ex}} = 465 \text{ nm}$ ) in DBAs reveals quenched fluorescence (Table 1), consistent with efficient ET, HT, and EnT, even in the conjugate with a tetrapeptide bridge. That  $\phi_f$  in **Cor-(Ala)<sub>4</sub>-PDI** is just three to seven times greater than that of **Cor-Ala-PDI** or **Cor-Phe-PDI** indicates that the tetrapeptide bridge does not substantially retard

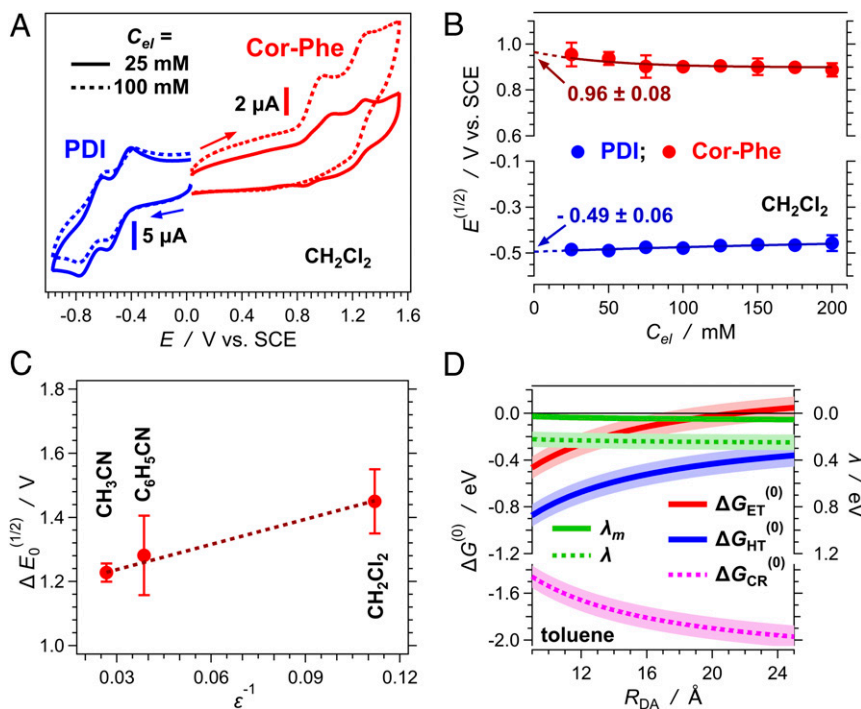


**Fig. 5.** Electrochemical analysis of **Cor-Phe** and **PDI** and thermodynamic parameters for the different CT processes. (A) Cyclic voltammograms of **Cor-Phe** and **PDI** in dichloromethane at 25 and 10 mM electrolyte concentrations ( $C_{el}$ ). (B) Dependence of the measured half-wave potentials [ $E^{(1/2)}$ ] on electrolyte concentration in dichloromethane extrapolated to neat solvent [ $E_0^{(1/2)}$ ] at  $C_{el} = 0 \text{ mM}$ . (C) Dependence of the neat-solvent potential difference [ $\Delta E_0^{(1/2)}(\epsilon)$ , Eq. 3] on solvent inverse dielectric constant ( $\epsilon^{-1}$ ). (D) Calculated driving forces for ET [ $-\Delta G_{\text{ET}}^{(0)}$ ], HT [ $-\Delta G_{\text{HT}}^{(0)}$ ], and CR [ $-\Delta G_{\text{CR}}^{(0)}$ ] as functions of donor–acceptor center-to-center distance ( $R_{\text{DA}}$ ) in toluene. The medium reorganization energy ( $\lambda_m$ ) is obtained from the Marcus two-sphere model (Eq. 5). Inner-sphere reorganization ( $0.13 \text{ eV} \lesssim \lambda_v \lesssim 0.26 \text{ eV}$ ) was estimated from Franck–Condon analyses of **Cor** and **PDI** fluorescence spectra.

ET and HT reactions in these conjugates (37, 58). The quantum yields indicate that deactivation of  $^1\text{PDI}^*$  via EnT and HT is more efficient than ET from  $^1\text{Cor}^*$  in the three DBA conjugates. The estimated Förster distance for  $^1\text{PDI}^* \rightarrow \text{Cor}$  EnT (46 Å) exceeds  $R_{\text{DA}}$  even for fully extended DBA conformations, consistent with efficient EnT. For HT to contribute to  $^1\text{PDI}^*$  decay, the HT rates must be comparable to those of EnT.

The exponential fluorescence decay times of  $^1\text{Cor}^*\text{-Phe}$  and  $^1\text{PDI}^*$  (4.5 and 4.7 ns, respectively; Table 1) correspond to radiative ( $k_f$ ) and nonradiative ( $k_{nr}$ ) decay rate constants  $k_f = 3.3 \times 10^8/k_{nr} = 1.9 \times 10^9 \text{ s}^{-1}$  for  $^1\text{Cor}^*\text{-Phe}$ , and  $k_f = 1.8 \times 10^9/k_{nr} = 3.2 \times 10^8 \text{ s}^{-1}$  for  $^1\text{PDI}^*$ . The three DBA conjugates exhibit multiexponential fluorescence decays, consistent with CT quenching by multiple DBA conformers (*SI Appendix*). The  $\phi_f$  values for **Cor-Ala-PDI** and **Cor-Phe-PDI** suggest that HT and ET rate constants ( $k_{\text{HT}}$  and  $k_{\text{ET}}$ ) exceed  $10^{10} \text{ s}^{-1}$ , but the time resolution of the fluorescence decay measurements ( $\sim 50$  ps) prevented observation of the fastest excited-state decay components. Consequently, we turned to femtosecond transient absorption (TA) spectroscopy to explore the earliest DBA excited-state events (Scheme 2).

TA spectroscopy reveals that Cor photoexcitation in DBA derivatives is followed by a picosecond rise of  $\text{PDI}^{\cdot-}$  and  $\text{Cor}^{\cdot+}$  650/850 nm transients (30), and there is concurrent bleaching of PDI ground-state absorptions (Figs. 6 and 7 *A–D*). As with fluorescence decay measurements, we observed heterogeneous TA kinetics for the DBA conjugates with decay components of 3–5, 40–60, and 160 ps (Table 1 and Fig. 8 *A–C*). In addition, a 1.4-ns decay was observed in **Cor-(Ala)<sub>4</sub>-PDI**. Importantly, these results suggest comparable donor–acceptor coupling pathways in all three DBA conjugates.

PDI photoexcitation is followed by a ground-state bleach, stimulated emission (SE), and a broad TA signal in the 650- to 850-nm region attributable to a singlet excited state (Fig. 6*B*). Within 1 to 2 ps in the DBA conjugates, the PDI stimulated emission disappears and the broad 650- to 850-nm  $^1\text{PDI}^*$  TA evolves into bands corresponding to  $\text{PDI}^{\cdot-}$  and  $\text{Cor}^{\cdot+}$  transients (Fig. 7 *E–G*). The dynamics are consistent with 1) photoinduced

HT to Cor and 2) EnT to Cor, followed by ET (Scheme 2). After these ultrafast changes in TA spectra, a further increase in the radical-ion TA accompanies growth of the **PDI** ground-state bleach (Fig. 7 *E–G*), consistent with the ET from  $^1\text{Cor}^*$  to **PDI** observed upon direct photoexcitation of the donor (Fig. 7 *A–C*). The observation of 30- to 70-ps ET upon photoexcitation of the acceptor indicates that  $^1\text{PDI}^*$  to **Cor** EnT accompanies the initial HT.

Global fitting can help distinguish HT from EnT–ET processes. In the case of HT, for example, the PDI ground-state bleach does not change during  $^1\text{PDI}^*$  TA decay. In the case of EnT, on the other hand, the PDI bleach recovers during  $^1\text{PDI}^*$  TA decay. The ET that follows EnT restores the PDI bleach but not SE or  $^1\text{PDI}^*$  TA.

Picosecond HT accompanies EnT that can be in the sub-picosecond time domain (Table 1). The heterogeneity of the kinetics reflects the diversity of conformational populations of DBA conjugates. For **Cor-Ala-PDI** and **Cor-Phe-PDI**, HT does not contribute substantially to  $^1\text{PDI}^*$  deactivation (Table 1), consistent with the large  $R_0$  and favorable orientation of transition dipole moments of the donor and acceptor. For **Cor-(Ala)<sub>4</sub>-PDI**, however, HT is a key deactivation channel for  $^1\text{PDI}^*$  (Table 1). Unlike **Cor-Ala-PDI** and **Cor-Phe-PDI**, the picosecond decay of  $^1\text{PDI}^*$  in **Cor-(Ala)<sub>4</sub>-PDI** appears to accompany TA growth of radical ions (Figs. 7*H* and 8 *D–F*), consistent with HT (Scheme 2). As CD shows, **Cor-(Ala)<sub>4</sub>-PDI** forms structures more tightly folded than those of **Cor-Ala-PDI** and **Cor-Phe-PDI** (Fig. 4 *A–C*).

The changes in TA spectra of the DBA conjugates when exciting the acceptor do not provide sufficient resolution for global fitting to determine the rates of competing HT and EnT processes. Nevertheless, comparison of exponential amplitudes [ $\alpha_i(\lambda)$ ] for sequential ET and charge recombination (CR) reveals that roughly 60% of **Cor-Ala-PDI** and **Cor-Phe-PDI** CT states originate from ET from  $^1\text{Cor}^*$  to PDI. For **Cor-(Ala)<sub>4</sub>-PDI**, on the other hand, 90% of the CT state is generated by direct HT from  $^1\text{PDI}^*$  to **Cor**. These findings indicate that **Cor-(Ala)<sub>4</sub>-PDI** EnT is much less efficient than that of either of the other two DBA conjugates.

While the calculated  $R_0$  value of 46 Å assumes random D and A transition-dipole-moment orientations, i.e.,  $\kappa = 2/3$ , this assumption may not be justified for these DBA conjugates, particularly **Cor-(Ala)<sub>4</sub>-PDI**. The CD results (Fig. 4*C*) and lower EnT efficiency suggest that **Cor-(Ala)<sub>4</sub>-PDI** adopts tight conformations in toluene where the PDI emission transition dipole moment is roughly orthogonal to that for  $\text{Cor } S_0 \rightarrow S_1$  absorption.

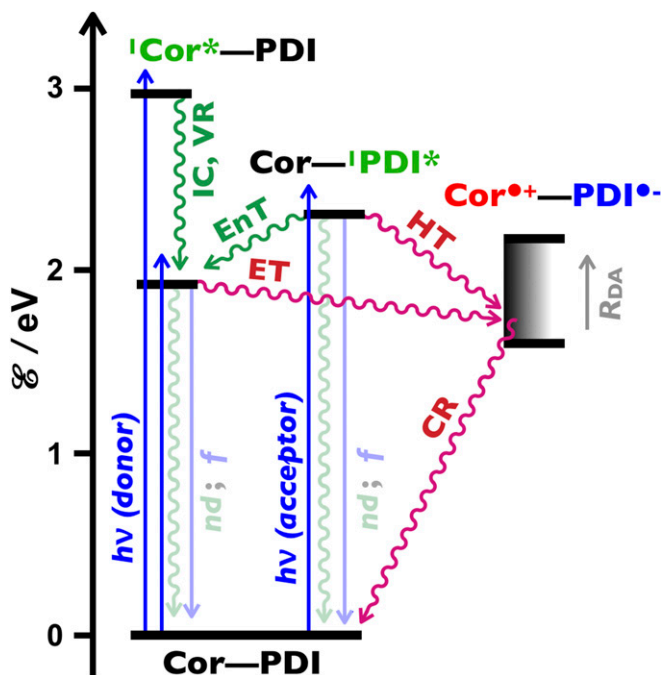
The DBA CR reactions (CR, Scheme 2) display multiexponential kinetics with time constants in the 0.4- to 2.6-ns time range. That the CR reactions are substantially slower than the excited-state charge separation processes (Table 1, Figs. 7*D* and 8 *A–C*) even though there is 1.0- to 1.4-eV greater free-energy release (Fig. 5*D*) is a clear indication of inverted driving-force behavior.

## Discussion

**ET Kinetics.** Semiclassical theory (Eq. 4) provides a platform for analysis of CT processes (Table 1) (59).

$$k_{\text{CT}} = \frac{2\pi}{\hbar\sqrt{4\pi\lambda k_{\text{B}}T}} |H_{\text{DA}}|^2 \exp\left(-\frac{(\Delta G_{\text{CT}}^{(0)} + \lambda)^2}{4\lambda k_{\text{B}}T}\right) \quad [4]$$

In Eq. 4,  $\lambda$  is the reorganization energy, comprising the inner ( $\lambda_{\text{i}}$ ) and medium ( $\lambda_{\text{m}}$ ) contributions ( $\lambda = \lambda_{\text{i}} + \lambda_{\text{m}}$ ). The solvent reorganization energy depends on the distance between donor and acceptor (Eq. 5) (59); the low dielectric constant of toluene constrains  $\lambda_{\text{m}}$  to 25–55 meV over a 9- to 25-Å span of  $R_{\text{DA}}$  (Fig. 5*D*). The uncertainty in  $S_{1/r}$ , obtained from the slope of the linear fit of  $\Delta E_0^{(1/2)}$  vs.  $\varepsilon^{-1}$  (Eq. 3*b* and Fig. 5*C*), has a relatively modest contribution to the uncertainty in  $\lambda$ :



**Scheme 2.** Jablonski diagram depicting photoinduced processes in **Cor-PDI** conjugates.

**Table 1. Fluorescence quantum yields ( $\phi_f$ ) and excited-state decay kinetics parameters for Cor, PDI, and three DBA conjugates**

	Cor-Phe	PDI	Cor-Ala-PDI	Cor-Phe-PDI	Cor-(Ala) <sub>4</sub> -PDI
$\phi_f(\text{Cor}) \times 10^2$ ( $\lambda_{\text{ex}} = 620$ nm)	15 ± 3	—	0.20 ± 0.07	0.33 ± 0.13	1.4 ± 0.3
$^1k_{\text{D}} \times 10^{-9}/\text{s}^{-1}$	0.22 ± 0.02	—	—	—	—
$\phi_f(\text{PDI}) \times 10^2$ ( $\lambda_{\text{ex}} = 465$ nm)	—	85 ± 6	0.02 ± 0.01	0.04 ± 0.01	0.11 ± 0.04
$^1k_{\text{D}} \times 10^{-9}/\text{s}^{-1}$	—	0.21 ± 0.02	—	—	—
$\lambda_{\text{ex}} = 400$ nm*					
$k_{\text{ET}} \times 10^{-9}/\text{s}^{-1}$	—	—	260 ± 60 (0.34) 24 ± 1 (0.53) 6.6 ± 0.2(0.13)	180 ± 30 (0.32) 16 ± 2 (0.53) 6.3 ± 0.5 (0.15)	360 ± 40 (0.34) 21 ± 3 (0.48) 6.6 ± 0.4 (0.07)
$k_{\text{CR}} \times 10^{-9}/\text{s}^{-1}$	—	—	2.5 ± 0.2 (0.42) 0.77 ± 0.04 (0.58)	1.4 ± 0.2 (0.52) 0.38 ± 0.08 (0.48)	0.72 ± 0.05 (0.11) 0.91 ± 0.3 (0.20) 0.58 ± 0.04 (0.80)
$\lambda_{\text{ex}} = 465$ nm*†					
$k_{\text{EnT}} \times 10^{-9}/\text{s}^{-1\dagger}$	—	—	1,700 ± 300 (0.50) 360 ± 40 (0.43)	1,400 ± 200 (0.33) 360 ± 30 (0.62)	1,500 ± 300 (0.34) 22 ± 2 (0.05) 7.8 ± 1.2 (0.04)
$k_{\text{HT}} \times 10^{-9}/\text{s}^{-1\dagger}$	—	—	190 ± 3 (0.06) 12 ± 3 (0.01)	27 ± 4 (0.04) <sup>§</sup> 20 ± 5 (0.01) <sup>§</sup>	260 ± 40 (0.06) <sup>§</sup> 230 ± 30 (0.48) <sup>§</sup> 7.4 ± 2 (0.03)
$k_{\text{ET}} \times 10^{-9}/\text{s}^{-1}$	—	—	280 ± 40 (0.34) 31 ± 5 (0.53) 7.0 ± 0.9 (0.13)	190 ± 40 (0.32) 10 ± 3 (0.57) 6.0 ± 0.6 (0.11)	180 ± 50 (0.40) 16 ± 2 (0.44) 4.4 ± 0.9 (0.06)
$k_{\text{CR}} \times 10^{-9}/\text{s}^{-1}$	—	—	1.8 ± 0.4 (0.67) 0.56 ± 0.08 (0.33)	3.5 ± 0.6 (0.17) 0.42 ± 0.13 (0.83)	0.54 ± 0.04 (0.10) 0.68 ± 0.09

Rate constants for energy transfer,  $k_{\text{EnT}}$ , hole transfer,  $k_{\text{HT}}$ , electron transfer,  $k_{\text{ET}}$ , and charge recombination,  $k_{\text{CR}}$  (for toluene), were obtained from global fit analyses, employing multiexponential functions for each of these CT processes,  $\Delta A(\lambda, t) = \sum_i \alpha_i(\lambda) \exp(-k_i t)$ . Values of rate constants from multiexponential fits are reported along with the corresponding normalized preexponential factors (in parentheses), i.e.,  $k_i(\alpha_i)$ , where  $\sum_i \alpha_i = 1$ .

\* $k_{\text{ET}}$  represents  $^1\text{Cor}^* + \text{PDI} \rightarrow \text{Cor}^{*\cdot} + \text{PDI}^{\cdot-}$  leading to simultaneous decay of the TA of  $^1\text{Cor}^*$  and the Cor stimulated emission ( $\text{SE}_{\text{Cor}}$ ) and growth of the PDI bleach ( $\text{B}_{\text{PDI}}$ ) and the TA of radical ions (Scheme 2 and Figs. 6–8).  $k_{\text{CR}}$  represents  $\text{Cor}^{*\cdot} + \text{PDI}^{\cdot-} \rightarrow \text{Cor} + \text{PDI}$  leading simultaneous decays of the TA of radical ions and recovery of ground-state bleaches of Cor and PDI,  $\text{B}_{\text{Cor}}$  and  $\text{B}_{\text{PDI}}$  (Scheme 2 and Figs. 6–8).

†When PDI is photoexcited,  $k_{\text{EnT}}$  represents  $\text{Cor} + ^1\text{PDI}^* \rightarrow ^1\text{Cor}^* + \text{PDI}$  leading to simultaneous decay of the TA of  $^1\text{PDI}^*$  and  $\text{SE}_{\text{PDI}}$ , growth of  $\text{B}_{\text{Cor}}$  and TA of  $^1\text{Cor}^*$ ,  $\text{SE}_{\text{Cor}}$ , and recovery of  $\text{B}_{\text{PDI}}$  (Scheme 2 and Figs. 6–8).  $k_{\text{HT}}$  represents  $\text{Cor} + ^1\text{PDI}^* \rightarrow \text{Cor}^{*\cdot} + \text{PDI}^{\cdot-}$  leading to simultaneous decay of the TA of  $^1\text{PDI}^*$  and  $\text{SE}_{\text{PDI}}$  and growth of  $\text{B}_{\text{Cor}}$  and the TA of radical ions (Scheme 2 and Figs. 6–8).

‡EnT and HT are competing processes for the decay of  $^1\text{PDI}^*$  (Scheme 2), i.e.,  $\Delta A(\lambda, t) = \sum_i \alpha_i(\lambda) \exp(-(k_{\text{EnT},i} + k_{\text{HT},i} + k_0^{(\text{PDI})}) t)$  where  $k_0^{(\text{PDI})} = 2.1 \times 10^8 \text{ s}^{-1}$  (measured using time-resolved fluorescence for PDI) accounts for  $^1\text{PDI}^*$  decay in the absence of Cor. Thus,  $\alpha_i^{(\text{EnT})} = \alpha_i k_{\text{EnT},i} (k_{\text{EnT},i} + k_{\text{HT},i})^{-1}$  and  $\alpha_i^{(\text{HT})} = \alpha_i k_{\text{HT},i} (k_{\text{EnT},i} + k_{\text{HT},i})^{-1}$  considering that  $k_0^{(\text{PDI})} \ll k_{\text{EnT},i}$  and  $k_0^{(\text{PDI})} \ll k_{\text{HT},i}$ .

§Similarities between  $k_{\text{HT},i}$  and  $k_{\text{HT},j}$  values (within the uncertainty of the analysis) are indicative of virtually identical HT rates for two populations that exhibit different EnT rates.

$$\lambda_m = \frac{e^2}{4\pi\epsilon_0} \left( \frac{1}{n^2} - \frac{1}{\epsilon} \right) \left( \frac{1}{2} S_{1/r} - \frac{1}{R_{\text{DA}}} \right). \quad [5]$$

For reactions far into the inverted driving-force region [i.e.,  $-\Delta G_{\text{CT}}^{(0)} \gg \lambda$ ], semiclassical theory underestimates nuclear tunneling contributions. The Marcus–Levich–Jortner model is more appropriate for this regime, as it takes specific account of nuclear tunneling (60) (Eq. 6):

$$k_{\text{CT}} = \frac{2\pi}{\hbar} |H_{\text{DA}}|^2 \frac{\exp\left(-\frac{\lambda_{\nu}}{\hbar\nu_{\text{C}}}\right)}{\sqrt{4\pi\lambda_{\nu}k_{\text{B}}T}} \sum_{j=0}^{\infty} \frac{\left(\frac{\lambda_{\nu}}{\hbar\nu_{\text{C}}}\right)^j}{j!} \exp\left(-\frac{(\Delta G_{\text{CT}}^{(0)} + \lambda_m + j\hbar\nu_{\text{C}})^2}{4\lambda_{\nu}k_{\text{B}}T}\right). \quad [6]$$

In Eq. 6,  $\nu_{\text{C}}$  represents a single high-frequency vibrational mode (or an average of frequencies). Values of inner-sphere reorganization

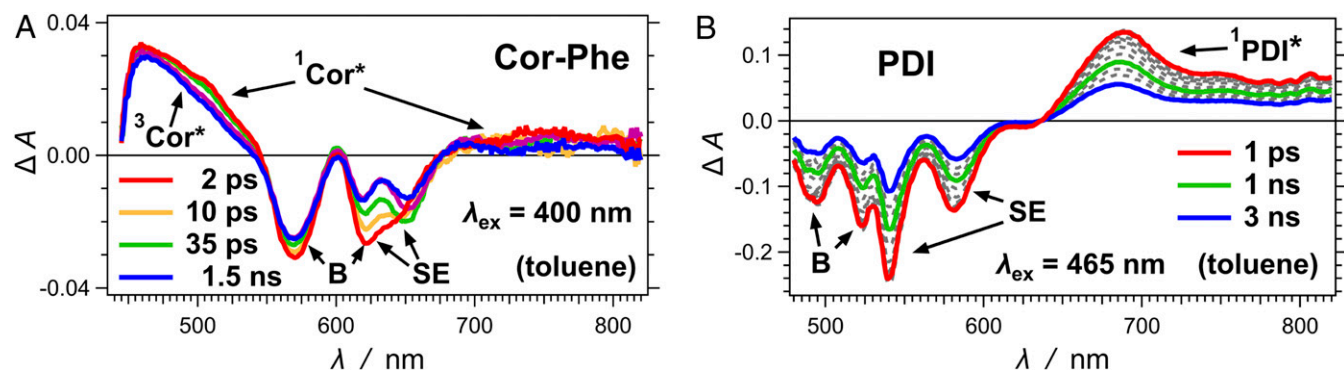


**Fig. 6.** TA spectra for (A) Cor-Phe,  $\lambda_{\text{ex}} = 400$  nm, and (B) PDI,  $\lambda_{\text{ex}} = 465$  nm for toluene (B, ground-state bleach; SE, stimulated emission).

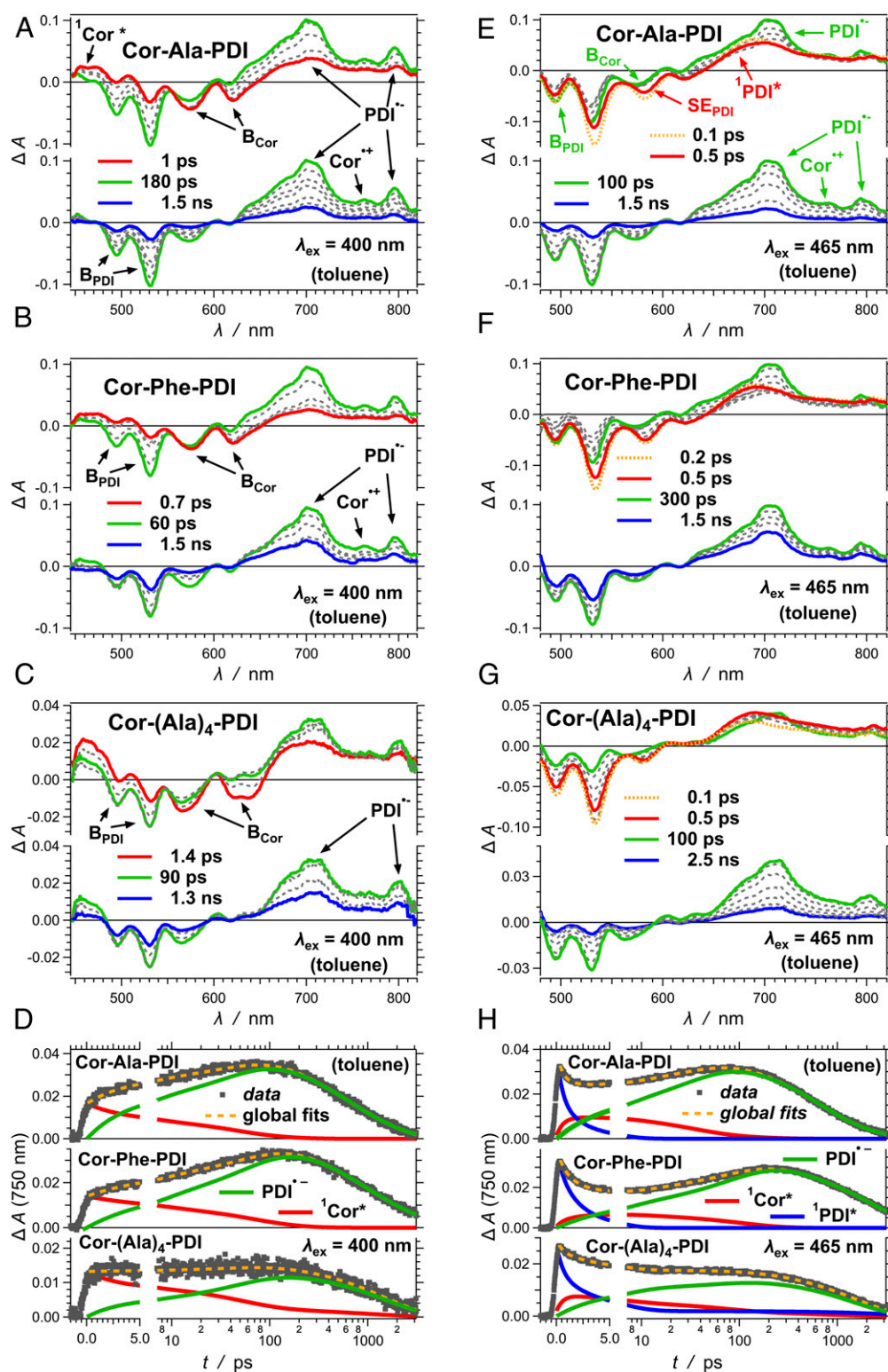


**Fig. 7.** TA dynamics for DBA conjugates upon excitation of (A–D) electron donor Cor at 400 nm and (E–H) electron acceptor PDI at 465 nm (pulse FWHM ~50 fs, 4  $\mu$ J per pulse). (A–C and E–G) TA spectra, showing the ground-state bleach of the electron donor,  $B_{\text{Cor}}$ , and of the electron acceptor,  $B_{\text{PDI}}$ , the stimulated emission of the acceptor,  $SE_{\text{PDI}}$ , and the TA of the radical ions. Spectral features of the two radical ions overlap in the 650- to 900-nm region. The molar extinction coefficient of  $\text{PDI}^{\cdot-}$  is much larger than that of  $\text{Cor}^{\cdot+}$ , making the  $\text{Cor}^{\cdot+}$  TA hard to see (D and H). TA kinetics traces recorded at 750 nm where  $\text{PDI}^{\cdot-}$ ,  ${}^1\text{Cor}^*$ , and  ${}^1\text{PDI}^*$  absorb; and the  $\Delta A(t)$  traces, which were obtained from global fits, show the kinetics of (D) photoinduced ET and the CR as well as (H) the photoinduced EnT and HT and the ET and CR that follow.

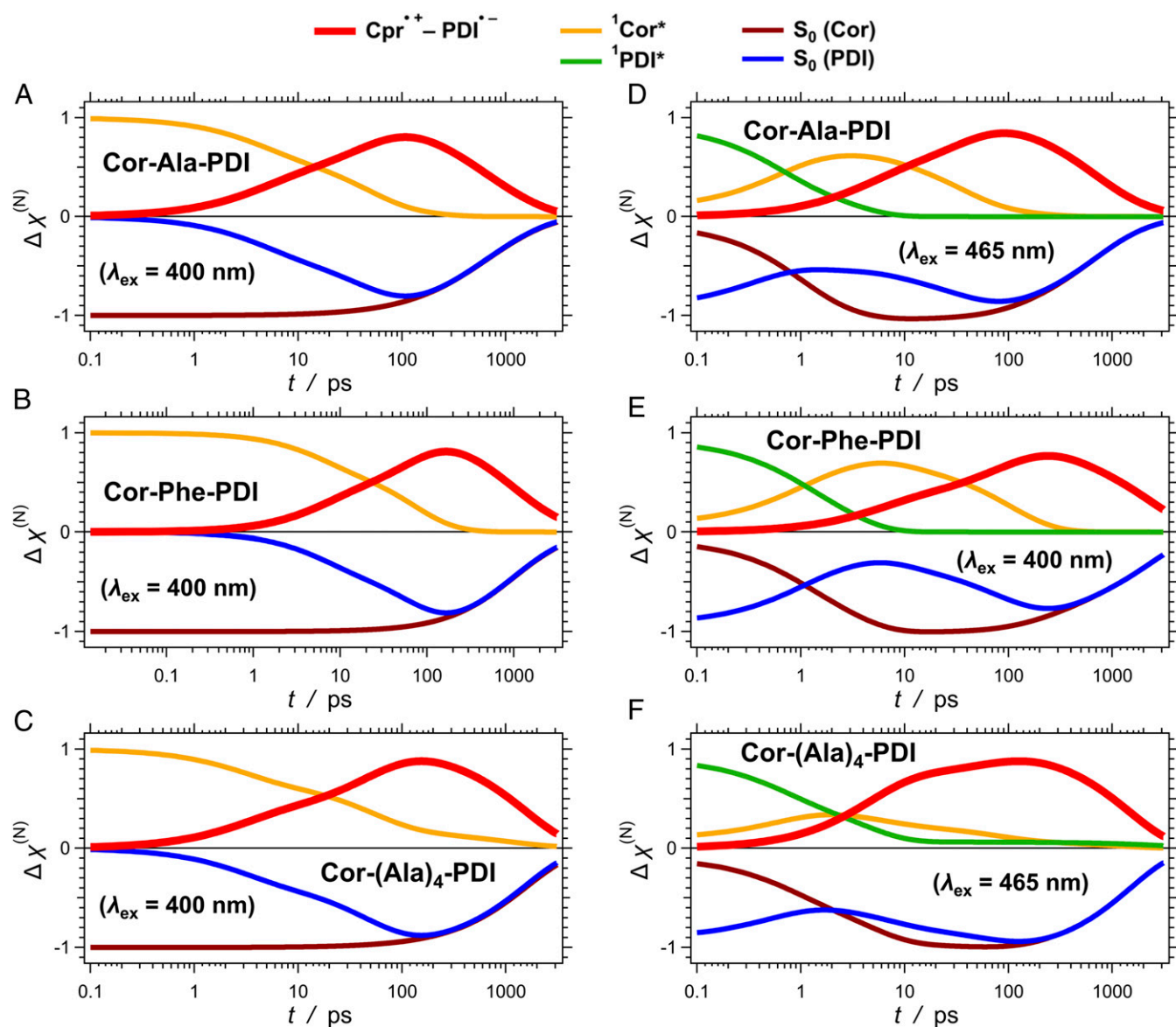


**Fig. 8.** Excited-state dynamics of Cor and PDI in the DBA conjugates extracted from TA analysis, showing the rises and the decays of the CT state,  $\text{Cor}^{\bullet+}\text{-PDI}^{\bullet-}$ , the locally excited states,  ${}^1\text{Cor}^*$  and  ${}^1\text{PDI}^*$ , and the ground-state bleaches,  $S_0(\text{Cor})$  and  $S_0(\text{PDI})$ . (A–C) Electron donor excitation (Cor, 400 nm); (D–F) electron acceptor excitation (PDI, 465 nm). Changes in molar fractions are normalized to the initial amplitudes of locally excited states, i.e.,  $\Delta\chi_i^{(N)}(t) = \Delta A_i(t)/(\Delta A({}^1\text{Cor}^*)_{t=0} + \Delta A({}^1\text{PDI}^*)_{t=0})$ .

energies for large polycyclic aromatic compounds tend to be less than 0.2 eV (61, 62). We can estimate  $\lambda_\nu$  contributions to **Cor** and **PDI** CT on the basis of their fluorescence spectra. In a simple one-electron approximation, the fluorescent excited states of **Cor** and **PDI** arise from the promotion of one electron from the bonding highest-energy occupied molecular orbital (HOMO) to the antibonding lowest-energy unoccupied molecular orbital (LUMO). The inner sphere reorganization energy associated with this process will be an upper limit to that involved in removal of one HOMO electron (oxidation) or delivery of one LUMO electron (reduction). Two-mode (one classical, one quantum) Franck–Condon analyses of the  ${}^1\text{Cor}$  and  ${}^1\text{PDI}$  fluorescence spectra (see *SI Appendix*) indicate that the upper limit to the inner-sphere reorganization energy for **Cor**–**PDI** CT is about 0.26 eV (0.18 eV quantum; 0.08 eV classical). The lower limit is likely to be no less than half of this value, suggesting that the range for  $\lambda_\nu$  is 0.13–0.26 eV (shaded region of the curve for  $\lambda$  in Fig. 5D).

The remaining unknown quantity in Eq. 6 is the electronic coupling strength,  $H_{DA}$ . The coupling along the (Cor)N–H $\cdots$ O=C–N–H $\cdots$ O(PDI) route can be estimated using the Beratan–Onuchic pathway model (37). This approach decomposes a pathway into a sequence of covalent bonds, hydrogen bonds, and through-space contacts, representing the overall coupling as repeated products of the coupling decays [ $\varepsilon^{(C)}$ ,  $\varepsilon^{(H)}$ ,  $\varepsilon^{(S)}$ ] for each step (Eq. 7):

$$H_{DA} = H_{DA}^{(0)} \prod_i \varepsilon_i^{(C)} \prod_i \varepsilon_i^{(H)} \prod_i \varepsilon_i^{(S)}. \quad [7]$$

The (Cor)N–H $\cdots$ O=C–N–H $\cdots$ O(PDI) pathway is composed of two covalent bonds [ $\varepsilon^{(C)} = 0.6$ ] and two H bonds. Coupling decays across the latter scale exponentially with distance ( $\varepsilon^{(H)} = 0.36 \exp[-1.7(r_i^{(H)} - 2.8)]$ ). The computed structure (Fig. 2C), optimized for toluene as a solvating medium, predicts that  $r_{(\text{Cor})\text{N-H}\cdots\text{O}}^{(H)} = 2.98$  Å and  $r_{\text{N-H}\cdots\text{O}(\text{PDI})}^{(H)} = 3.02$  Å. The predicted coupling along the (Cor)N–H $\cdots$ O=C–N–H $\cdots$ O(PDI) pathway is  $H_{DA} = 0.024$

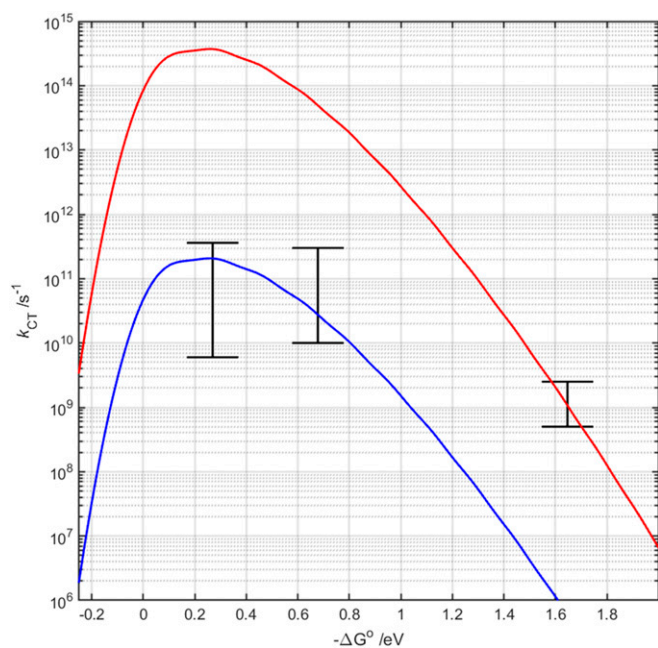


**Fig. 9.** Driving-force dependence of Cor/PDI CT rate constants in toluene (black) and driving-force dependence calculated using Eq. 6 with the following parameters:  $\lambda_m = 38$  meV;  $\lambda_v = 260$  meV (180 meV quantum; 80 meV classical);  $h\nu_c = 0.156$  eV;  $H_{DA} = 3.1$  meV (blue);  $H_{DA} = 131$  meV (red).

$H_{DA}^{(0)}$ , where  $H_{DA}^{(0)}$  represents the electronic coupling when the donor and acceptor are in contact.

The electrochemical and optical properties of Cor and PDI (Fig. 5), the calculated structures (Fig. 2), and the solvent characteristics permit estimates of all parameters for the semiclassical analysis (Eq. 6) except  $H_{DA}^{(0)}$ . The ET and HT rate constants (Table 1) are consistent with nonadiabatic reactions ( $H_{DA} = 3.1$  meV, Fig. 9), corresponding to the pathway-model prediction of 130 meV for the coupling at contact. The CR rate constants, however, are much greater than predicted for this coupling strength. The electrostatic attraction between  $\text{Cor}^+$  and  $\text{PDI}^-$  in toluene is likely to drive a conformational change that brings the ions into contact or possibly separated by a single solvent molecule. If we assume that  $H_{DA} = 0.13$  eV, the rate constant calculated using Eq. 6 is much closer to the experimental value (Fig. 9), although it is possible that conformational dynamics contribute to the observed recombination rate constants. Moreover, polarization of the wavefunctions in the radical ion pair could enhance electronic coupling for CR. Prior evaluations of electronic coupling across a single toluene molecule suggest a value of  $\sim 2.5$  meV (63). Investigations of CR in radical ion pairs indicate coupling strengths of  $\sim 1.2$  meV for solvent-separated ion pairs, and  $\sim 0.12$  eV for contact ion pairs (64).

### Concluding Remarks

The close similarity of the CT dynamics for all three DBA conjugates (Table 1) suggests comparable electronic coupling pathways.

The strong hydrogen-bonding propensities of pyrrole NH groups are crucial for shortening the coupling pathway between the donor and the middle of the bridge. Another equally important structural feature is the tendency of the PDI imide carbonyls to interact with hydrogen-bond donors on the bridge (Fig. 2). These hydrogen-bonding capabilities of the donor and acceptor are exploited in stabilizing the conformation that features the  $(\text{Cor})\text{NH}\cdots\text{O}=\text{C}-\text{NH}\cdots\text{O}=\text{C}(\text{PDI})$  tunneling pathway motif. A single amide from the middle of the bridge hydrogen bonds with both the donor and acceptor, providing relatively strong electronic coupling while keeping the  $\text{CT } R_{DA} < 20$  Å for  $\Delta G_{\text{ET}}^{(0)} < 0$  (Fig. 5D). The heterogeneity of HT and ET kinetics (Figs. 7 D–F and 8 D–F) is consistent with the structural fluctuations observed for these compact DBA conjugates. Future investigations could address the role of vibrational excitation of the bridge in modulating ET and HT kinetics (65).

Folded structures with intramolecular hydrogen-bonding networks can greatly enhance the rates of DBA CT reactions. ET rate maxima result when the driving force matches the reorganization energy [ $-\Delta G_{\text{CT}}^{(0)} \sim \lambda$ ] (Fig. 9). CT reactions of Cor/PDI DBA complexes in toluene ( $\epsilon = 2.38$ ) involve very little solvent reorganization (25–55 meV) coupled with a relatively modest inner-sphere contribution (130–260 meV). Consequently, only very small driving forces are required to achieve optimal CT reactions. It has long been recognized that photoinduced charge-separation reactions exhibit a weak dependence on solvent polarity despite the fact that both  $\Delta G_{\text{CT}}^{(0)}$  and  $\lambda_m$  are extremely sensitive to solvent dielectric constant (66). For charge-separation reactions, reducing solvent polarity lowers both  $-\Delta G_{\text{CT}}^{(0)}$  and  $\lambda_m$ , leading to relatively weak solvent dependences. CR reactions, on the other hand, tend to become more deeply inverted as solvent polarity decreases, favoring long-lived charge separation. In the Cor/PDI DBA conjugates, this effect was partially negated by structural changes that enhanced CR electronic coupling.

Our structure–function analysis of DBA conjugates with peptide bridges has revealed structural features that could assist in the design of efficient CT systems. When an electron donor and acceptor contain substituents capable of hydrogen bonding in aprotic nonpolar (but polarizable) environments, intramolecular hydrogen-bond interactions can provide more efficient CT electronic coupling pathways. We emphasize that relatively small DBA conjugates, such as the ones reported here, can serve as functional models for understanding the fundamental factors that control the dynamics of ET and HT reactions in natural biomolecules as well as complex molecular machines.

**Data Availability.** All study data are included in the article and/or supporting information.

**ACKNOWLEDGMENTS.** This work was supported by the National Science Centre, Poland (Grants HARMONIA 2016/22/M/ST5/00431 and PRELUDIUM 2016/23/N/ST5/00052), and the NSF (Grants CHE 1800602 and MPS AGEP-GRS to J.A.C.). A.S. and H.J. were supported by National Science Centre Grant 2017/25/B/ST5/01011 and Wrocław Centre for Networking and Supercomputing Grant 299. Research at the California Institute of Technology was supported by the National Institute of Diabetes and Digestive and Kidney Diseases of the NIH under Award R01DK019038. The content is solely the responsibility of the authors and does not necessarily represent the official views of the NIH.

- N. Nelson, C. F. Yocum, Structure and function of photosystems I and II. *Annu. Rev. Plant Biol.* **57**, 521–565 (2006).
- T. Ritz, A. Damjanović, K. Schulten, The quantum physics of photosynthesis. *ChemPhysChem* **3**, 243–248 (2002).
- S. Y. Reece, J. M. Hodgkiss, J. Stubbe, D. G. Nocera, Proton-coupled electron transfer: The mechanistic underpinning for radical transport and catalysis in biology. *Philos. Trans. R. Soc. Lond. B Biol. Sci.* **361**, 1351–1364 (2006).
- D. R. Weinberg *et al.*, Proton-coupled electron transfer. *Chem. Rev.* **112**, 4016–4093 (2012).
- S. Y. Reece, D. G. Nocera, Proton-coupled electron transfer in biology: Results from synergistic studies in natural and model systems. *Annu. Rev. Biochem.* **78**, 673–699 (2009).
- J. Jortner, M. Bixon, T. Langenbacher, M. E. Michel-Beyerle, Charge transfer and transport in DNA. *Proc. Natl. Acad. Sci. U.S.A.* **95**, 12759–12765 (1998).
- M. S. Reagan, C. Pittenger, W. Siede, E. C. Friedberg, Characterization of a mutant strain of *Saccharomyces cerevisiae* with a deletion of the RAD27 gene, a structural homolog of the RAD2 nucleotide excision repair gene. *J. Bacteriol.* **177**, 364–371 (1995).
- A. Sancar, L. A. Lindsey-Boltz, K. Unsal-Kaçmaz, S. Linn, Molecular mechanisms of mammalian DNA repair and the DNA damage checkpoints. *Annu. Rev. Biochem.* **73**, 39–85 (2004).
- J. D. Rochaix, Regulation of photosynthetic electron transport. *Biochim. Biophys. Acta* **1807**, 375–383 (2011).

10. J. R. Winkler, H. B. Gray, Electron flow through metalloproteins. *Chem. Rev.* **114**, 3369–3380 (2014).
11. H. B. Gray, J. R. Winkler, Long-range electron transfer. *Proc. Natl. Acad. Sci. U.S.A.* **102**, 3534–3539 (2005).
12. J. R. Winkler, H. B. Gray, Long-range electron tunneling. *J. Am. Chem. Soc.* **136**, 2930–2939 (2014).
13. V. I. Vullev, From biomimesis to bioinspiration: What's the benefit for solar energy conversion applications? *J. Phys. Chem. Lett.* **2**, 503–508 (2011).
14. A. M. Scott, A. B. Ricks, M. T. Colvin, M. R. Wasielewski, Comparing spin-selective charge transport through donor-bridge-acceptor molecules with different oligomeric aromatic bridges. *Angew. Chem. Int. Ed. Engl.* **49**, 2904–2908 (2010).
15. A. M. Scott, M. R. Wasielewski, Temperature dependence of spin-selective charge transfer pathways in donor-bridge-acceptor molecules with oligomeric fluorenone and p-phenylethynylene bridges. *J. Am. Chem. Soc.* **133**, 3005–3013 (2011).
16. E. A. Weiss, M. R. Wasielewski, M. A. Ratner, Molecules as wires: Molecule-assisted movement of charge and energy. *Top. Curr. Chem.* **257**, 103–133 (2005).
17. M. Gilbert, B. Albinsson, Photoinduced charge and energy transfer in molecular wires. *Chem. Soc. Rev.* **44**, 845–862 (2015).
18. M. Wolffs *et al.*, Helical aromatic oligoamide foldamers as organizational scaffolds for photoinduced charge transfer. *J. Am. Chem. Soc.* **131**, 4819–4829 (2009).
19. X. Li *et al.*, Photoinduced electron transfer and hole migration in nanosized helical aromatic oligoamide foldamers. *J. Am. Chem. Soc.* **138**, 13568–13578 (2016).
20. B. Giese, Electron transfer through DNA and peptides. *Bioorg. Med. Chem.* **14**, 6139–6143 (2006).
21. H.-A. Wagenknecht, "Preface" in *Charge Transfer in DNA: From Mechanism to Application*, H.-A. Wagenknecht, Ed. (Wiley, 2005), pp. vii–viii.
22. G. Jones 2nd, X. Zhou, V. I. Vullev, Photoinduced electron transfer in alpha-helical polypeptides: Dependence on conformation and electron donor-acceptor distance. *Photochem. Photobiol. Sci.* **2**, 1080–1087 (2003).
23. T. A. Zeidan, Q. Wang, T. Fiebig, F. D. Lewis, Molecular wire behavior in pi-stacked donor-bridge-acceptor tertiary arylureas. *J. Am. Chem. Soc.* **129**, 9848–9849 (2007).
24. M. Son, B. Fimmel, V. Dehm, F. Würthner, D. Kim, Folding-induced modulation of excited-state dynamics in an oligophenylene-ethynylene-tethered spiral perylene bisimide aggregate. *ChemPhysChem* **16**, 1757–1767 (2015).
25. L. Sebaou, V. Maurizot, T. Granier, B. Kauffmann, I. Huc, Aromatic oligoamide  $\beta$ -sheet foldamers. *J. Am. Chem. Soc.* **136**, 2168–2174 (2014).
26. D. M. Guldi, K.-D. Asmus, Electron transfer from C76 (C2v) and C78 (D2) to radical cations of various arenes: Evidence for the Marcus inverted region. *J. Am. Chem. Soc.* **119**, 5744–5745 (1997).
27. T. R. Prytkova, I. V. Kurnikov, D. N. Beratan, Coupling coherence distinguishes structure sensitivity in protein electron transfer. *Science* **315**, 622–625 (2007).
28. J. L. Sessler, M. Sathiosatham, C. T. Brown, T. A. Rhodes, G. Wiederrecht, Hydrogen-bond-mediated photoinduced electron-transfer: Novel dimethylaniline-anthracene ensembles formed via Watson-Crick base-pairing. *J. Am. Chem. Soc.* **123**, 3655–3660 (2001).
29. P. J. de Rege, S. A. Williams, M. J. Therien, Direct evaluation of electronic coupling mediated by hydrogen bonds: Implications for biological electron transfer. *Science* **269**, 1409–1413 (1995).
30. L. Flamigni *et al.*, New and efficient arrays for photoinduced charge separation based on perylene bisimide and corroles. *Chem. Eur. J.* **14**, 169–183 (2008).
31. M. Tasior *et al.*, Energy- and electron-transfer processes in corrole-perylenebisimide-triphenylamine array. *J. Phys. Chem. C* **112**, 19699–19709 (2008).
32. R. Orłowski *et al.*, Self-assembling corroles. *Chem. Commun. (Camb.)* **51**, 8284–8287 (2015).
33. R. Orłowski *et al.*, Hydrogen bonds involving cavity NH protons drives supramolecular oligomerization of amido-corroles. *Chem. Eur. J.* **23**, 10195–10204 (2017).
34. R. Orłowski *et al.*, Covalently linked bis(amido-corroles): Inter- and intramolecular hydrogen-bond-driven supramolecular assembly. *Chem. Eur. J.* **25**, 9658–9664 (2019).
35. R. Orłowski, D. Gryko, D. T. Gryko, Synthesis of corroles and their heteroanalogues. *Chem. Rev.* **117**, 3102–3137 (2017).
36. P. Wu, L. Brand, Resonance energy transfer: Methods and applications. *Anal. Biochem.* **218**, 1–13 (1994).
37. D. N. Beratan, J. N. Betts, J. N. Onuchic, Protein electron transfer rates set by the bridging secondary and tertiary structure. *Science* **252**, 1285–1288 (1991).
38. R. Armen, D. O. V. Alonso, V. Daggett, The role of alpha-, 3(10)-, and pi-helix in helix-coil transitions. *Protein Sci.* **12**, 1145–1157 (2003).
39. G. Jones, P. Willett, R. C. Glen, A. R. Leach, R. Taylor, Development and validation of a genetic algorithm for flexible docking. *J. Mol. Biol.* **267**, 727–748 (1997).
40. N. Gresh, G. Tiraboschi, D. R. Salahub, Conformational properties of a model alanyl dipeptide and of alanine-derived oligopeptides: Effects of solvation in water and in organic solvents—a combined SIBFA/continuum reaction field, ab initio self-consistent field, and density functional theory investigation. *Biopolymers* **45**, 405–425 (1998).
41. I. Mandal, S. Paul, R. Venkatramani, Optical backbone-sidechain charge transfer transitions in proteins sensitive to secondary structure and modifications. *Faraday Discuss.* **207**, 115–135 (2018).
42. R. Langen *et al.*, Electron tunneling in proteins: Coupling through a beta strand. *Science* **268**, 1733–1735 (1995).
43. X. Ru, P. Zhang, D. N. Beratan, Assessing possible mechanisms of micrometer-scale electron transfer in heme-free *Geobacter sulfurreducens* pili. *J. Phys. Chem. B* **123**, 5035–5047 (2019).
44. S. Upadhyayula *et al.*, Permanent electric dipole moments of carboxyamides in condensed media: What are the limitations of theory and experiment? *J. Phys. Chem. B* **115**, 9473–9490 (2011).
45. S. D. Straight *et al.*, Photochromic control of photoinduced electron transfer. Molecular double-throw switch. *J. Am. Chem. Soc.* **127**, 2717–2724 (2005).
46. M. J. Frisch *et al.*, Gaussian 09, Revision E.01 (Gaussian Inc., Wallingford, CT, 2009).
47. D. Rehm, A. Weller, Kinetics of fluorescence quenching by electron and H-atom transfer. *Isr. J. Chem.* **8**, 259–271 (1970).
48. D. Bao *et al.*, Electrochemical oxidation of ferrocene: A strong dependence on the concentration of the supporting electrolyte for nonpolar solvents. *J. Phys. Chem. A* **113**, 1259–1267 (2009).
49. J. B. Derr *et al.*, Multifaceted aspects of charge transfer. *Phys. Chem. Chem. Phys.* **22**, 21583–21629 (2020).
50. Y. Fang, Z. Ou, K. M. Kadish, Electrochemistry of corroles in nonaqueous media. *Chem. Rev.* **117**, 3377–3419 (2017).
51. J. Shen *et al.*, Electrochemistry and spectroelectrochemistry of meso-substituted free-base corroles in nonaqueous media: Reactions of (cor)H3, [(Cor)H4]+, and [(Cor)H2]–. *Inorg. Chem.* **45**, 2251–2265 (2006).
52. E. M. Espinoza *et al.*, Practical aspects of cyclic voltammetry: How to estimate reduction potentials when irreversibility prevails. *J. Electrochem. Soc.* **166**, H3175–H3187 (2019).
53. D. Bao *et al.*, Dipole-mediated rectification of intramolecular photoinduced charge separation and charge recombination. *J. Am. Chem. Soc.* **136**, 12966–12973 (2014).
54. A. Purc *et al.*, Gating that suppresses charge recombination—the role of mono-N-arylated diketopyrrolopyrrole. *J. Am. Chem. Soc.* **138**, 12826–12832 (2016).
55. M. Krzeszewski *et al.*, Dipole effects on electron transfer are enormous. *Angew. Chem. Int. Ed. Engl.* **57**, 12365–12369 (2018).
56. S. K. Lee *et al.*, Electrochemistry, spectroscopy and electrogenerated chemiluminescence of perylene, terylene, and quaterylene diimides in aprotic solution. *J. Am. Chem. Soc.* **121**, 3513–3520 (1999).
57. M. Kuss-Petermann, O. S. Wenger, Unusual distance dependences of electron transfer rates. *Phys. Chem. Chem. Phys.* **18**, 18657–18664 (2016).
58. A. Heck *et al.*, Charge transfer in model peptides: Obtaining Marcus parameters from molecular simulation. *J. Phys. Chem. B* **116**, 2284–2293 (2012).
59. R. A. Marcus, N. Sutin, Electron transfers in chemistry and biology. *Biochim. Biophys. Acta* **811**, 265–322 (1985).
60. M. Bixon, J. Jortner, Non-Arrhenius temperature-dependence of electron-transfer rates. *J. Phys. Chem.* **95**, 1941–1944 (1991).
61. X. Amashukeli, N. E. Gruhn, D. L. Lichtenberger, J. R. Winkler, H. B. Gray, Inner-sphere electron-transfer reorganization energies of zinc porphyrins. *J. Am. Chem. Soc.* **126**, 15566–15571 (2004).
62. X. Amashukeli, J. R. Winkler, H. B. Gray, N. E. Gruhn, D. L. Lichtenberger, Electron-transfer reorganization energies of isolated organic molecules. *J. Phys. Chem. A* **106**, 7593–7598 (2002).
63. J. M. Nadeau, M. Liu, D. H. Waldeck, M. B. Zimmt, Hole transfer in a C-shaped molecule: Conformational freedom versus solvent-mediated coupling. *J. Am. Chem. Soc.* **125**, 15964–15973 (2003).
64. I. R. Gould, R. H. Young, R. E. Moody, S. Farid, Contact and solvent-separated geminate radical ion pairs in electron-transfer photochemistry. *J. Phys. Chem.* **95**, 2068–2080 (1991).
65. Z. Lin *et al.*, Modulating unimolecular charge transfer by exciting bridge vibrations. *J. Am. Chem. Soc.* **131**, 18060–18062 (2009).
66. H. Oevering *et al.*, Long-range photoinduced through-bond electron transfer and radiative recombination via rigid nonconjugated bridges: Distance and solvent dependence. *J. Am. Chem. Soc.* **109**, 3258–3269 (1987).